Journal of Advanced Ceramics
2024, **13**(11): 1823–1834
https://doi.org/10.26599/JAC.2024.9220993

Research Article

Defect chemistry and thermal conductivity of the $\varepsilon SmO_{1.5}\cdot(1-\varepsilon)ZrO_2$ ($0.2 \le \varepsilon \le 0.65$) ceramics: Effect of the nonstoichiometry

Zhixue Qu[1,✉], Tong Zhang[1], Wei Pan[2]

[1] *Key Laboratory of Advanced Functional Materials, Education Ministry of China, College of Materials Science and Engineering, Beijing University of Technology, Beijing 100124, China*
[2] *State Key Laboratory of New Ceramics and Fine Processing, School of Materials Science and Engineering, Tsinghua University, Beijing 100084, China*

Received: September 10, 2024; Revised: October 18, 2024; Accepted: October 22, 2024

Abstract: Rare-earth zirconate pyrochlores, which exhibit various interesting properties, especially low thermal conductivity, are of great interest. Nonstoichiometry is an effective strategy involving defect engineering to reduce the thermal conductivity of materials. In this work, a long series of solid solutions, $\varepsilon SmO_{1.5}\cdot(1-\varepsilon)ZrO_2$ (ε = 0.200, 0.250, 0.350, 0.400, 0.450, 0.500, 0.525, 0.550, 0.600, and 0.650), were designed and synthesized to investigate the effects of nonstoichiometry on the structural evolution, defect chemistry, and thermal conductivity of $SmO_{1.5}$–ZrO_2 system across the entire pyrochlore phase field and phase transition regions. The similarity of all the Raman spectra provides an incredible opportunity to confirm the structural details and evolution of pyrochlore and defective fluorite, as well as the emergence of the expected point defects. A new solution mechanism concerning nonstoichiometry was proposed and confirmed by analyzing the variations in the experimental density and Raman spectra. The thermal conductivities of all the samples were measured, and investigated in terms of the phonon-scattering theory. The results show that the nonstoichiometry with $SmO_{1.5}$ excess is more effective in reducing the thermal conductivity to an extremely low value of approximately 1 W/(m·K), which can be attributed to the dramatic decrease in the average acoustic velocity in addition to the strong phonon scattering of Zr ion vacancies and oxygen vacancies. On the other hand, the nonstoichiometry with ZrO_2 excess significantly reduces the thermal conductivity at room temperature, but conversely leads to a slight increase of it above 200 °C. The former variation can be attributed to the phonon scattering of the 8*a* interstitial oxygen ions, which has a similar effectiveness to the defects on the $SmO_{1.5}$-rich side. The latter variation may be attributed to the Umklapp scattering of phonons.

Keywords: nonstoichiometry; pyrochlore; rare-earth zirconate; thermal conductivity; defect chemistry

1 Introduction

Rare-earth zirconates with an ideal stoichiometry of $Ln_2Zr_2O_7$ (Ln = lanthanides) have been widely investigated as potential top coat materials for thermal barrier coating (TBC) applications [1–5]. To further reduce the thermal conductivity of $Ln_2Zr_2O_7$, several effective strategies, such as doping approaches [6–11] and high-entropy alloying [12–17], have been explored. All these strategies involve defect engineering; that is, various point defects, such as vacancies and substitutions, are introduced into the lattice of materials to increase the scattering of the phonons, thereby reducing the thermal conductivity [18].

Nonstoichiometry is also an effective strategy involving defect engineering to reduce the thermal conductivity of materials. Deviation from the stoichiometric composition creates different types and populations of point defects due to electroneutrality and enhances lattice distortion and disorder, which decreases the thermal conductivity of materials. Wu *et al.* [19] measured the thermal conductivities of ceramics in the $GdO_{1.5}$–ZrO_2 system within the full compositional range and concluded that the thermal conductivity decreases from one of two end compounds (Gd_2O_3 and ZrO_2) with increasing doping content of their counterparts. Interestingly, the thermal conductivity of the stoichiometric compound $Gd_2Zr_2O_7$ right in the middle with a pyrochlore structure is not exactly the minimum. The value is slightly greater than those of the surrounding compositions at all temperatures, which may be attributed to the variation in the thermal conductivity of the compositions within the pyrochlore phase field. However, they did not investigate this interesting variation further. Recently, Chen *et al.* [20] carried out a theoretical calculation in terms of the Slack model on the thermal conductivities of the nonstoichiometric compositions close to $Gd_2Zr_2O_7$ and verified the calculation results with experimental data. Unfortunately, the experimental thermal conductivities at relatively lower temperatures are not consistent with the calculation results, whereas the experimental data at much higher temperatures show an abnormal increase which may be attributed to the increasing importance of radiative transport rather than phonon conduction. In addition, the samples they prepared were sintered at 1600 °C, which indicates that all these samples have transformed into a fluorite structure instead of a pyrochlore structure. Some earlier efforts were also devoted to the thermal conductivities of other nonstoichiometric rare-earth zirconate systems. Liu *et al.* reported the thermal conductivities of the

✉ Corresponding author.
E-mail: quzhixue@bjut.edu.cn

nonstoichiometric compositions on the ZrO_2-rich side in $NdO_{1.5}$–ZrO_2 [21] and $SmO_{1.5}$–ZrO_2 [22] systems. A similar behavior of thermal conductivity can be observed in both systems: The thermal conductivities of the nonstoichiometric compositions are lower at low temperatures but higher at high temperatures than those of the stoichiometric composition. However, the authors overlooked this interesting variation. On the other hand, Guo *et al.* [23] indicated that the competing influences of the different crystal structures of the samples in Liu *et al.*'s work [21] on thermal conductivity hindered the investigation of the effect of nonstoichiometry and emphasized that all the investigated samples should share identical structures for the sake of comparison. Therefore, they prepared two near-stoichiometric compositions on the ZrO_2-rich side of the $NdO_{1.5}$–ZrO_2 system which are identical in structure to the stoichiometric compound $Nd_2Zr_2O_7$, and measured the thermal conductivities of the three samples. The results demonstrated that the thermal conductivity of the measured samples decreases with increasing deviation from the stoichiometric composition over the entire investigated temperature range. Despite these efforts, there is still little systematic research concerning the variation in thermal conductivity with the nonstoichiometry of rare-earth zirconates, especially for compositions throughout the pyrochlore phase field.

In the phase diagrams of $LnO_{1.5}$–ZrO_2 systems [24,25], a pyrochlore phase field with a significant homogeneity range exists in each system with the lighter lanthanide element from La to Gd. In light of the phase diagrams calculated by Wang *et al.* [24,25], the composition range of the pyrochlore phase field shows a roughly increasing trend with lanthanide contraction, and $GdO_{1.5}$–ZrO_2 system was expected to possess the widest pyrochlore phase field, which seems to be the preferred choice for investigating the effect of nonstoichiometry on the thermal conductivity of rare-earth zirconate pyrochlores. However, other reports [26–28] have demonstrated that $SmO_{1.5}$–ZrO_2 system may actually be a system with a wider homogeneity range of pyrochlore. Tabira and Withers [28] determined the composition range of the pyrochlore phase field in the $SmO_{1.5}$–ZrO_2 system to be from 38.5 to 55 mol% $SmO_{1.5}$ at 1500 °C, which is significantly wider than that of the $GdO_{1.5}$–ZrO_2 system reported by Jorba [26] and Lakiza *et al.* [27]. Moreover, the upper critical temperature below which the pyrochlore phase exists steadily is approximately 1530 °C for $GdO_{1.5}$–ZrO_2 system [24], whereas it is approximately 2025 °C in the case of $SmO_{1.5}$–ZrO_2 system [28]. The low thermal stability temperature makes it difficult to prepare and further investigate samples with pyrochlore structures in $GdO_{1.5}$–ZrO_2 system. In contrast, the wider homogeneity range and sufficiently higher thermal stability temperature of the pyrochlore phase field in $SmO_{1.5}$–ZrO_2 system offer an opportunity for us to systemically investigate the thermal conductivity variation with the nonstoichiometry of rare-earth zirconates throughout the pyrochlore phase field, which is the main aim of this work.

On the other hand, nonstoichiometry results in a highly complex defect chemical reaction. Stanek *et al.* [29] carried out a theoretical calculation via atomistic simulation to predict the defect chemical reactions for the nonstoichiometry of an extensive series of $A_2B_2O_7$ (A = La, Pr, Nd, Sm, Eu, Gd, Y, Er, Yb, and Lu; B = Ti, Ru, Mo, Sn, Zr, and Pb) and concluded that there are two competing defect mechanisms involving A cation vacancies and oxygen interstitials for some compositions with BO_2 excess, whereas oxygen vacancies are expected to be the compensating defects to accommodate the excess $AO_{1.5}$. Defect chemistry is essential for understanding the thermal conduction behavior of materials. Unfortunately, there has been no further experimental evidence to validate the above simulation results. This work aims to confirm the defect chemistry in $SmO_{1.5}$–ZrO_2 system due to nonstoichiometry and to further interpret the variation in thermal conductivity with deviation from stoichiometry.

2 Experimental

2.1 Compositional design

In the phase diagram of $SmO_{1.5}$–ZrO_2 system, the pyrochlore phase field is a dome-like region with the ideal stoichiometric compound $Sm_2Zr_2O_7$ right in the middle and two narrow two-phase (pyrochlore + fluorite) regions varying with temperature appear on either side of it, all of which are surrounded by a vast field of a defective fluorite phase. Although extensive studies have been carried out [24–26,30], many contradictions still exist in the literature with respect to the boundaries of the pyrochlore phase field as well as the two-phase regions. Jorba [26] reported a wide composition range of pyrochlore phase field of 23–43 mol% Sm_2O_3 (37.4–60.1 mol% $SmO_{1.5}$) at 1450 °C, in contrast to the corresponding value of 38.5–55 mol% $SmO_{1.5}$ at 1500 °C reported by Tabira and Withers [28]. On the contrary, the phase diagram of $SmO_{1.5}$–ZrO_2 system calculated by Wang *et al.* [24,25] shows a distinctly narrower pyrochlore phase field, particularly on the ZrO_2-rich side. These contradictions could be attributed to the difficulty in distinguishing between pyrochlore and defective fluorite structures. Determining the exact boundaries of the pyrochlore phase field is essential for preparing and investigating samples over the entire composition range of the pyrochlore phase field.

For this purpose, the compositions investigated in this work were designed to vary across the reported pyrochlore phase field and even the two-phase regions. The phase diagrams calculated by Wang *et al.* [24,25] were adopted as references to predict the possible phases of the designed compositions since they supply more sufficient data at various temperatures than the methods in the other literature do. As a higher sintering temperature is more beneficial for improving the densification of the samples for the sake of thermal conductivity measurement, the designed compositions in this work were compared with the critical compositions of various phase fields at 1600 °C from the phase diagram, as shown in Fig. 1.

The stoichiometric compound $Sm_2Zr_2O_7$ corresponding to ε = 0.500 in the formula $\varepsilon SmO_{1.5}\cdot(1-\varepsilon)ZrO_2$ can be considered the origin of the nonstoichiometry and the reference compound for the structure and thermal conductivity investigations. From this starting composition, two sets of compositions corresponding to different directions of deviation can be designed. On the ZrO_2-rich side, the composition with ε = 0.450 would nearly lie at the left-hand boundary of the pyrochlore phase field on the basis of the phase diagram calculated by Wang *et al.* [24,25]. In contrast, it can be deduced from the wide composition range of the pyrochlore phase field at 1500 °C reported by Tabira and Withers [28] that the compositions with ε = 0.450 and even ε = 0.400 would exist as a single pyrochlore phase rather than as a pyrochlore + fluorite mixture, as indicated in Fig. 1. The identification of the phases of these two compositions helps to confirm the exact boundary of the pyrochlore phase field. In addition, the composition with ε = 0.350 is expected to be a pyrochlore + fluorite mixture, whereas the compositions with ε = 0.200 and 0.250 are unequivocally in the form of a single defective fluorite, which can be compared with the pyrochlores in terms of structural evolution and thermal conductivity variation. On the

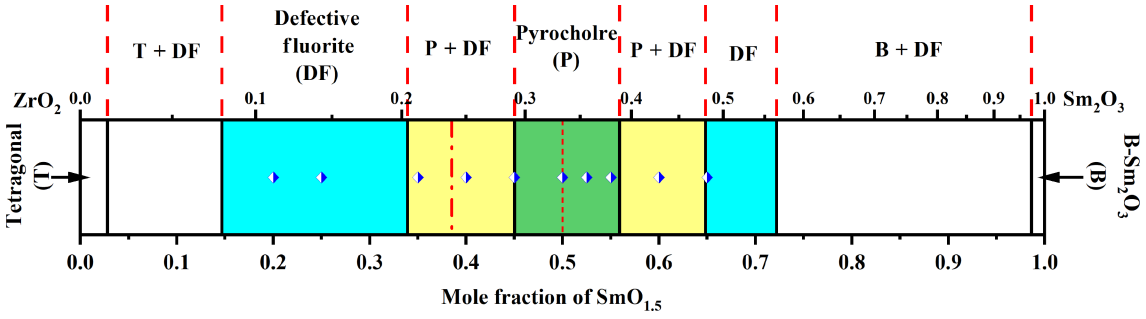

Fig. 1 Compositional slice at 1600 °C from the phase diagram calculated by Wang *et al.* [24,25] with designed compositions investigated in this work as symbolized by white-blue diamonds. The scale of top *x*-axis represents mole fraction of Sm_2O_3, in contrast to mole fraction of $SmO_{1.5}$ on bottom *x*-axis. For comparison, the left-hand boundary of pyrochlore phase field at 1500 °C reported by Tabira and Withers [28] is labeled in the figure with a red dash-dot line.

$SmO_{1.5}$-rich side, the compositions with ε = 0.525 and 0.550 are supposed to fall in the phase field of the pyrochlore, although the latter is likely to be the critical composition, as inferred from Tabira and Withers' report [28]. Moreover, the composition with ε = 0.600 is considered a pyrochlore + fluorite mixture, whereas the composition with ε = 0.650 is close to the boundary of the fluorite phase field which probably crystallizes as a fluorite phase. These two compositions are designed for comparison.

2.2 Materials processing

The ten designed compositions $\varepsilon SmO_{1.5}\cdot(1-\varepsilon)ZrO_2$ (ε = 0.200, 0.250, 0.350, 0.400, 0.450, 0.500, 0.525, 0.550, 0.600, and 0.650) were synthesized via a chemical coprecipitation method. Sm_2O_3 powder (purity ≥ 99.9%; Rare Earth Co., Ltd., China) and $ZrOCl_2\cdot 8H_2O$ powder (purity ≥ 99.0%; Beijing Chem. Indus. Co., Ltd., China) were used as the sources of Sm and Zr. Sm_2O_3 powder was calcined at 1000 °C for 10 h to eliminate hydroxide and/or carbonate to ensure accurate compositions. The freshly heated Sm_2O_3 powder was then dissolved in diluted nitric acid, while $ZrOCl_2\cdot 8H_2O$ powder was dissolved in deionized water. These two solutions were mixed in the expected stoichiometric ratio and stirred for 30 min. The fully mixed solution was then added dropwise into an excess solution of ammonia water with vigorous stirring and ultrasonic oscillating to obtain gel-like precipitates. After that, the precipitates were filtered and washed with deionized water three times, followed by washing with ethanol twice. The washed precipitates were then dried via a rotary evaporator and calcined at 800 °C for 5 h. The prepared powder was sieved through 400 mesh and pressed into pellets via uniaxial cold pressing (100 MPa), followed by isostatic cold pressing (200 MPa). The compacts were sintered at 1600 °C for 10 h in air.

2.3 Structure characterizations

The phases of all ten compositions were identified via an X-ray diffractometer (XRD; D/max-RB, Rigaku, Japan) using nickel-filtered Cu Kα radiation. The lattice parameters were extrapolated from slow-step XRD scan data via the least-squares method, and the theoretical densities were thereby estimated in terms of the lattice parameters and various supposed defect chemical reactions in this work.

The Raman spectra of all ten compositions were recorded at room temperature on a microscopic confocal Raman spectrometer (RM2000, Renishaw, UK) using an argon ion laser with radiation at 514.5 nm. The laser beam was focused on a freshly polished surface under a microscope with a spot width of ~2 μm. The signal was collected at a rate of 600 cm^{-1}/30 s with an accuracy of 1 cm^{-1} and accumulated for a triple scan. Several spots were detected for each sample to ascertain the homogeneity of the samples.

2.4 Property measurement

The thermal conductivity (κ') was calculated from three parameters, namely, the thermal diffusivity (λ), heat capacity (c_p), and bulk density (ρ), via Eq. (1):

$$\kappa' = \lambda \cdot c_p \cdot \rho \tag{1}$$

Among these parameters, thermal diffusivity was measured via the laser flash method (LFA 427, Netzsch, Germany). The samples were machined to be disk-shaped, and the surfaces are parallel, with a thickness of approximately 1 mm and a diameter of 10 mm. The surfaces of the samples on both sides were coated with colloidal graphite to ensure full absorption of the laser flash and maximum emissivity, as well as to minimize radiative heat transport. The measurement was carried out in a pure Ar atmosphere from room temperature to 800 °C at intervals of 200 °C. A model considering radiation and pulse correction [31] was used to determine the thermal diffusivity with a standard deviation of less than 2%. The heat capacity was calculated according to the Neumann-Kopp rule, that is, the weighted sum of the heat capacity values of its constituent oxides (Sm_2O_3 and ZrO_2) obtained from Ref. [32]. It has been verified that the experimental values are within approximately ±3% of the corresponding calculated values [33]. The bulk density was measured via the Archimedes method with an immersion medium of deionized water. The overall uncertainty of the thermal conductivity was estimated to be less than ±5%. Moreover, taking the effect of micropores into consideration, the thermal conductivities were corrected to the values for fully dense samples (κ) via the Maxwell relation (Eq. (2)) [34]:

$$\kappa'/\kappa = 1 - \frac{3}{2}\phi \tag{2}$$

where ϕ is the porosity of the measured sample, which was calculated in terms of the theoretical density via the solution mechanism confirmed in this work.

The longitudinal (v_l) and transverse (v_t) acoustic velocities were measured via an ultrasonic pulser/receiver instrument (5900PR, Panametrics, USA) by determining the transmission interval between two parallel surfaces of the sample. The average acoustic velocity ($\bar{v}$) was then calculated from the longitudinal and transverse acoustic velocities (Eq. (3)) [35]:

$$\bar{v} = 3^{1/3}\left(\frac{1}{v_l^3} + \frac{2}{v_t^3}\right)^{-1/3} \tag{3}$$

3 Results and discussion

3.1 Phase identification and lattice parameters

XRD patterns of all the investigated compositions from a continuous scan, as shown in Fig. 2, reveal that all the diffraction lines correspond to the spectra of either pyrochlore or defective fluorite, with no appreciable peaks of the other additional phases. To distinguish the pyrochlore from the defective fluorite, the peaks (311), (331), and (511) corresponding to the superlattice of the pyrochlore structure were marked with a star in the pattern of the stoichiometric composition with ε = 0.500. All the other patterns were compared and identified carefully in terms of the peak shape and occurrence of the superlattice peaks. The results are summarized in Table 1.

As expected, the compositions with ε = 0.200 and 0.250 are in the form of defective fluorite without any trace of the superlattice peaks. It looks as if the composition with ε = 0.350 also takes the phase of defective fluorite, but nearly invisible peaks corresponding to (331) and (511) planes can be observed from the partially enlarged details of the pattern from 35° to 47° at the top of Fig. 2, which indicates the presence of a trace of pyrochlore phase in addition to the defective fluorite. Interestingly, the compositions with ε = 0.400 and 0.450 were confirmed to be single pyrochlore phase through the remarkable superlattice peaks and no indication of the coexistence of defective fluorite. This provides convincing evidence to support the wide composition range of the pyrochlore phase field in $SmO_{1.5}$–ZrO_2 system, which is in accordance with the reports by Jorba [26] and Tabira and Withers [28] but contradicts the results of Wang *et al.* [24,25]. Moreover, in light of the case of ε = 0.350, the existence of a fairly narrow pyrochlore + fluorite region on the ZrO_2-rich side, which was not detected by Tabira and Withers [28], has been verified.

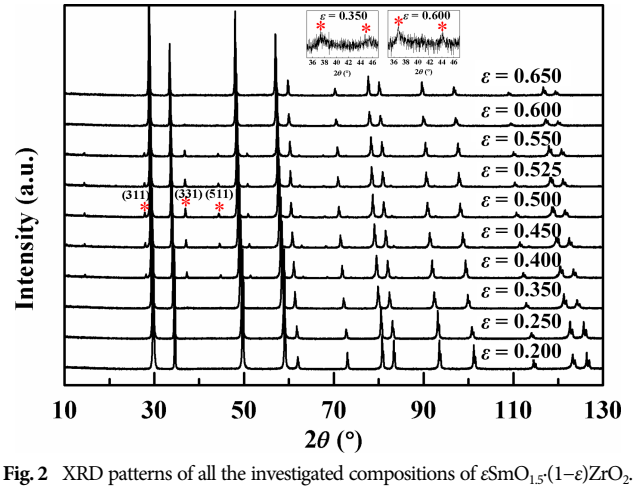

Fig. 2 XRD patterns of all the investigated compositions of $\varepsilon SmO_{1.5}$·$(1-\varepsilon)ZrO_2$. The small peaks labeled with a star originate from the superlattice of pyrochlore phase. The insets at the top of the figure are partially enlarged details from 35° to 47° for the compositions with ε = 0.350 and 0.600, respectively. The weak peaks suggest presence of pyrochlore phases.

Table 1 Phase identification and densities of all the investigated compositions

Composition ε	Expected phase	Identified phase	I_{331}/I_{max} (%)	Density (g/cm^3)
0.200	DF	DF	—	6.277
0.250	DF	DF	—	6.341
0.350	DF + P	DF + P	0.977	6.459
0.400	(DF + P)/P	P	3.231	6.512
0.450	P	P	4.312	6.507
0.500	P	P	5.469	6.440
0.525	P	P	4.390	6.280
0.550	P	P	3.944	6.278
0.600	DF + P	DF + P	1.487	6.109
0.650	DF	DF	—	5.949

Note: DF means defective fluorite, and P means pyrochlore.

On the $SmO_{1.5}$-rich side, the compositions with ε = 0.525 and 0.550 are also in the form of a single pyrochlore phase, as expected. These compositions, together with the compositions with ε = 0.400, 0.450, and 0.500, constitute a complete series of samples throughout the pyrochlore phase field. Furthermore, in contrast to the case of ε = 0.350, it is easy to identify the coexistence of the pyrochlore and defective fluorite phases at ε = 0.600 from the weak but visible superlattice peaks in the inset of Fig. 2 and the unusual shape of the other peaks with an excessively high right shoulder. As an example, the peak at approximately 78° from a step XRD scan was fitted by two overlapping pseudo-Voigt functions, as shown in Fig. 3. These two peaks are generally attributed to the pyrochlore and defective fluorite phases, respectively. As one of the two end compositions of the tie line in the two-phase region of $SmO_{1.5}$-rich side, the defective fluorite phase is expected to be richer in Sm ions than the pyrochlore phase. Since the larger ion radius of Sm ion expands the lattice of the defective fluorite phase, the stronger peak at a lower angle (Peak 1) should be ascribed to the defective fluorite phase, whereas the weaker peak at a higher angle (Peak 2) corresponds to the pyrochlore phase. Moreover, the composition with ε = 0.650 is clearly the single defective fluorite phase.

To verify the structural regularity of the pyrochlore structure, the relative intensities of the representative superlattice peak (331) to the strongest peak at approximately 30° for the compositions containing the pyrochlore phase were calculated and are shown in Table 1. The value of $I_{(331)}/I_{max}$ first increases and then decreases with increasing ε, with a maximum at ε = 0.500, that is, the stoichiometric composition. In other words, the stoichiometric compound $Sm_2Zr_2O_7$ has a more ideal pyrochlore phase, and the nonstoichiometry of this system disorders the lattice of materials, resulting in deviation from the ideal pyrochlore phase.

Figure 2 also shows that all the diffraction peaks systematically shift toward lower 2θ angles with increasing ε. For clarity, the diffraction peak at approximately 58°, which corresponds to either (622) for pyrochlore or (311) for fluorite, was individually step

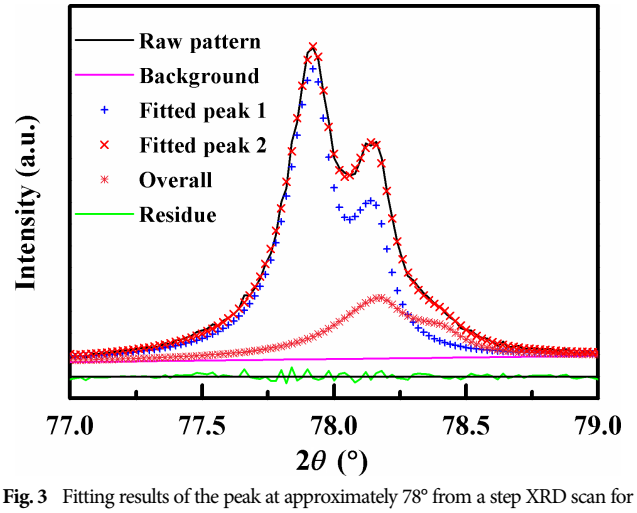

Fig. 3 Fitting results of the peak at approximately 78° from a step XRD scan for the composition with ε = 0.600. Fitted peak 1 may correspond to defective fluorite, whereas peak 2 is likely to be from pyrochlore phase.

scanned for each composition and compared in Fig. 4(a). The remarkable shift shown suggests significant lattice expansion with increasing content of $SmO_{1.5}$, which may be attributed to the larger ion radius of Sm ions.

Figure 4(b) shows the lattice parameters of all the compositions extrapolated from slow-step XRD data via the least-squares method. The error bars are too small in comparison with the symbol size to be shown in the figure. For comparison with pyrochlore, twice the lattice parameter, $2a$, is plotted in the figure for the defective fluorite. In the case of the composition with ε = 0.600, the lattice parameters were calculated from the fitting results for the pyrochlore and defective fluorite phases. Unfortunately, the diffraction peaks of the pyrochlore phase at ε = 0.350 are too weak to be separated from those of the defective fluorite phase appropriately, so the lattice parameter of the pyrochlore phase at this composition is not shown in the figure. The increase in the lattice parameter of the pyrochlore phase with increasing ε is also in line with Vagard's slope constructed from the data for compositions with a defective fluorite phase, which coincides with the results of Wang *et al.* [24,25]. The nearly linear variation in the lattice parameters across both the pyrochlore and defective fluorite phase fields may imply that the phase transition from pyrochlore to defective fluorite does not lead to a dramatic structural change.

3.2 Raman spectroscopy and structure analysis

Raman spectroscopy was used to characterize the structural details further, which is considered to be more sensitive to the structural disorder of pyrochlores, especially the disorder in the anion sublattice. Figure 5 shows the Raman spectra of all the investigated compositions. The first striking feature of the data is the similar spectra of the compositions with a defective fluorite structure to those with a pyrochlore phase, which is quite different from the results of XRD analysis. Factor group analysis has predicted six Raman active modes for the vibration spectra of $A_2B_2O_7$ pyrochlores in contrast to only one Raman active mode for the ideal fluorite, which can be represented as Eqs. (4) and (5):

$$\Gamma_P = A_{1g} + E_g + 4T_{2g} \quad (4)$$

$$\Gamma_F = T_{2g} \quad (5)$$

It was expected that the compositions with a defective fluorite phase should have spectra with only one band, which should be completely different from those with a pyrochlore phase. However, Fig. 5 clearly shows that more than one band appears in the spectra of all the compositions with a defective fluorite phase, which closely resembles that of the neighboring composition with a pyrochlore phase. Similar cases have been observed in $NdO_{1.5}$–ZrO_2 system [36] and other rare-earth zirconates with defective fluorite phases [37,38]. This may imply that the transition from pyrochlore to defective fluorite does not completely alter the crystal structure of materials and that some short-range ordered domains exist in a long-range disordered lattice. This has been evidenced by recent neutron total scattering investigations of pyrochlore and defective fluorite structures [39–41], which suggest that a local order configuration with weberite-like orthorhombic nanodomains exists in the lattice of various long-range structures, such as disordered pyrochlore, defective fluorite, and even their amorphous counterparts under irradiation, as characterized by XRD analysis. By neutron total scattering methods, Drey *et al.* [41] analyzed the structural details of the nonstoichiometric $NdO_{1.5}$–ZrO_2 system on the ZrO_2-rich side and revealed that at a long-range scale, the samples undergo a rapid pyrochlore–defective fluorite transition with deviation from stoichiometry at a very narrow compositional range of approximately 31 mol% $NdO_{1.5}$, whereas at a short-range scale, the pyrochlore gradually transforms to a weberite-like phase. The gradually increasing short-range ordered domains, instead of fully disordered defective fluorite, may result in the Raman spectra of the defective fluorite being similar to those of the pyrochlore phase.

Another interesting feature of the data is the continuously varying profiles of all the spectra with composition. This is not surprising if the continuous increase in the short-range ordered domains is considered. However, all the spectra are not consistent with those of typical A_3BO_7 websites, the exact mechanism of which remains unclear. In any event, the continuity of the variation in the spectra with composition provides an incredible opportunity to confirm how nonstoichiometry affects the structural details of the materials as well as to probe the structural evolution during the order–disorder transition from pyrochlore to defective fluorite.

Following the well-established analysis of the spectrum of $Sm_2Zr_2O_7$ (ε = 0.500), all the spectra can easily be resolved into several similar bands. As shown in Fig. 5, nine possible bands, labeled P1–P9, were observed by fitting the curves with Lorentz functions, among which the bands P5 and P8 appear only in the spectra of the compositions on the ZrO_2-rich side and $SmO_{1.5}$-rich side, respectively.

The vibrational modes were assigned through comprehensive

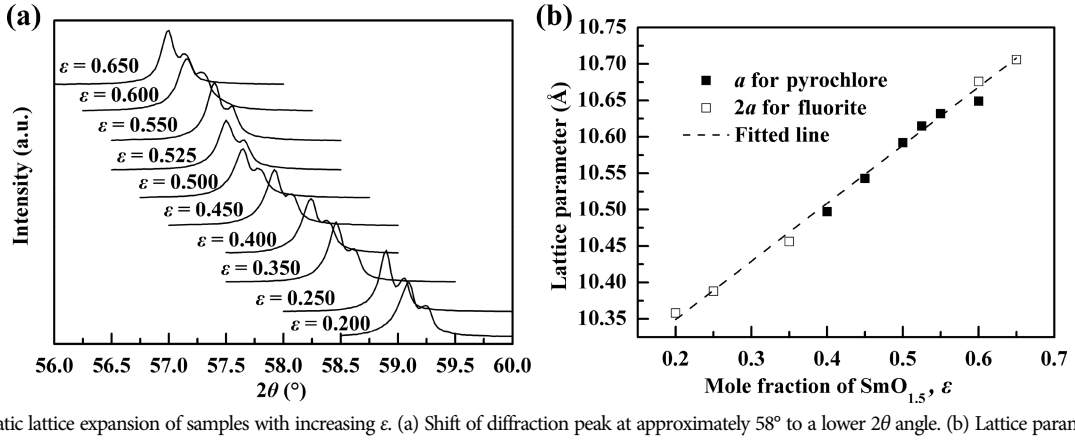

Fig. 4 Systematic lattice expansion of samples with increasing ε. (a) Shift of diffraction peak at approximately 58° to a lower 2θ angle. (b) Lattice parameters of all the compositions extrapolated from slow-step XRD data. Error bars are too small in comparison with symbol size to be shown here. For comparison with pyrochlore, twice lattice parameter, $2a$, is plotted for defective fluorite.

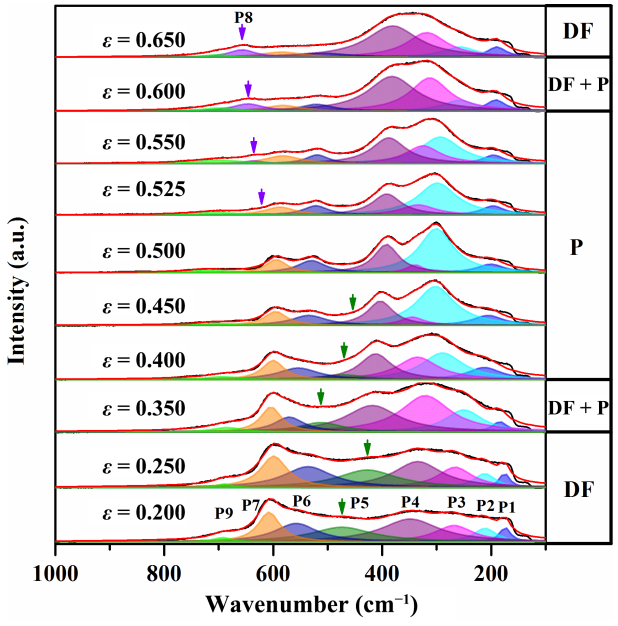

Fig. 5 Raman spectra of all the compositions. The curves were fitted by several Lorentz functions which were color-coded and labeled P1–P9. The arrows with olive and violet colors indicate appearances of the bands P5 and P8, respectively.

analysis and comparison with the literature on the Raman spectra of various pyrochlores [42–45]. According to previously reported polarized Raman measurements [42,45], the band P6 can be explicitly assigned to the A_{1g} mode. In contrast, the assignment of the other vibrational modes is quite difficult because of the overlaps of various modes as well as the occasional presence of some bands of uncertain origin. For example, there is disagreement in the literature on the assignment of the E_g mode. Compared with the well-resolved spectra of stannate pyrochlores and the results of force field calculations [42,44,46], the band P4, rather than the band P2 or P3, is identified as the E_g mode in this work. After the E_g mode assignment, the bands P2, P3, and P7 are clearly assigned to three of the four T_{2g} modes. With respect to the fourth T_{2g} mode, there are also several different opinions. The low-lying band P1, which is usually considered to have T_{2g} symmetry in titanate pyrochlores, has been proven not to be a fundamental frequency and may be attributed to the possible appearance of IR modes in Raman spectra involving A and O vibrations due to the lowering of local symmetry [42,47]. The bands P5 and P8, which appear only on one side, may be attributed to some additional modes due to certain point defects induced by nonstoichiometry. The band P5 at approximately 450 cm^{-1} was thought to be the fourth fundamental T_{2g} mode in our previous work [43] but was not observed visibly. We now consider it is the expected additional T_{2g} mode originating from the occupancy of the 8*a* vacancy site. Moreover, the origin of the band P8 is also expected to be some newly generated point defects, which will be discussed in the next section. Ultimately, the only available band left, the band P9, is identified as the fourth fundamental T_{2g} mode, which is consistent with the results of the titanate and stannate pyrochlores as well as the ab initio density functional calculations [45].

The Raman shifts of the nine fitted bands are summarized in Fig. 6, which shows an interesting trend of variation with composition, especially in the pyrochlore phase field and phase transition regions. The figure shows a remarkable shift to a higher wavenumber for most of the bands during the defective fluorite–pyrochlore transition, which is more pronounced on the

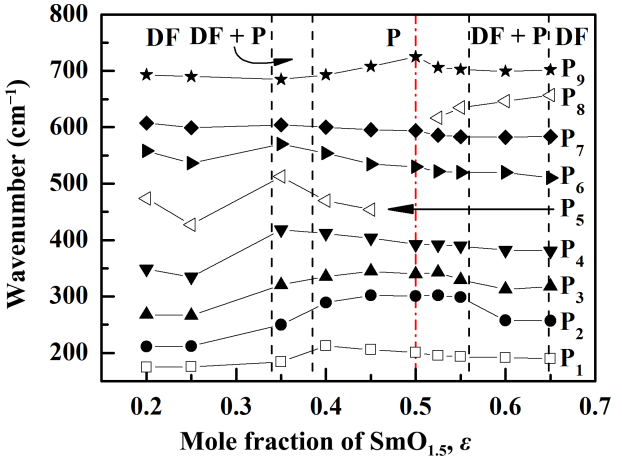

Fig. 6 Raman shifts of various fitted bands as a function of mole fraction of $SmO_{1.5}$. The phase boundaries verified by XRD are indicated in figure to confirm the variation due to the phase transition. The connecting line is a guide to the eye.

ZrO_2-rich side. This may imply that the bonds become tighter when the material transforms from defective fluorite to a pyrochlore structure. This finding also confirms the onset of pyrochlore formation, i.e., the boundaries of the pyrochlore phase field and two-phase regions. Moreover, in the phase field of the pyrochlore structure, the variation in the Raman shift of different bands varies. The bands P2 and P3 show similar variations on each side of the stoichiometric composition, which involves a slight decrease in wavenumber with deviation from stoichiometry, followed by an abrupt drop at the edge of the two-phase region. The variation in the band P9 is similar but distinguished by a dramatically increased frequency at the stoichiometric composition, followed by a continuous decrease on each side. The band P8, which only appears on the $SmO_{1.5}$-rich side, is the only band showing an increase in wavenumber with increasing $SmO_{1.5}$ excess. Moreover, all the remaining bands exhibit a continuous decrease in wavenumber with increasing content of $SmO_{1.5}$ after the abrupt rise in the left phase transition region, which runs on even the right fluorite phase field.

The variation in the Raman shift can be attributed to the vibrations of various bonds. Owing to the stronger bonding strength of B–O bond than that of A–O bond, the bands with relatively low wavenumbers in the Raman spectra of $A_2B_2O_7$ pyrochlores are expected to be chiefly related to the vibrations of the bonds between A and O ions, whereas those with relatively high wavenumbers may be attributed to the vibrations of the bonds between B and O ions. This can also be evidenced by the variation in the relative intensities of the bands with low and high wavenumbers in Fig. 5. Therefore, in light of the similar variations in the Raman shifts, the bands P2 and P3 can be considered to involve the vibrations of Sm–O and/or O–Sm–O bonds. The slight decrease in wavenumber on the left side of the stoichiometric composition for the bands P2 and P3 can be attributed to the further deviation of O^{2-} ions from Sm^{3+} ions due to the increasing content of Zr^{4+} ions which are more electronegative than Sm^{3+} ions. Moreover, the similar decrease in wavenumber on the right side of the stoichiometric composition may be attributed to lattice expansion due to the increasing number of Sm^{3+} ions with larger ionic radii. On the other hand, the bands P4–P7 may involve the vibrations of Zr–O and/or O–Zr–O bonds, and the increasing content of Sm^{3+} ions and the consequent lattice expansion may be responsible for the steady decrease in wavenumber. Among them, the band P5 shows a

more notable variation but disappears at the stoichiometric composition, which suggests that it is not a fundamental frequency of the pyrochlore structure. The most likely origin is the interstitial oxygen ion occupying the 8*a* vacancy site, which is surrounded by four Zr ions. The band P8, which also disappears at the stoichiometric composition, may originate from a certain point defect introduced by the excess $SmO_{1.5}$. The high wavenumber, as well as its unusual increase with $SmO_{1.5}$ excess, suggests the possibility of strengthened Zr–O bonds due to the emergence of the expected point defect. The band P9 is supposed to stem from the vibrations of Zr–O and/or O–Zr–O bonds involving the distortion of ZrO_6 octahedra. In $A_2B_2O_7$ pyrochlore, 48*f* O ion is off-centered within an A_2B_2 tetrahedron and is coordinated by a free positional parameter *x*, which is quite different from 8*b* O ion with a fixed site in the center of an A_4 tetrahedron. The positional parameter *x* varies between 0.3125 and 0.375 with the origin selected at the B cation, which determines the distortion of BO_6 octahedron as well as AO_8 cube. Tabira and Withers [28] reported the *x* values for $\varepsilon SmO_{1.5}\cdot(1-\varepsilon)ZrO_2$ system and demonstrated that nonstoichiometry on both sides increases *x* from a minimum value of 0.342 for a stoichiometric composition with $\varepsilon = 0.500$ to a higher value that approaches 0.375 as in the fluorite structure. As shown in Fig. 7, the increase in *x* with nonstoichiometry leads to much more distortion of ZrO_6 octahedra as well as an increase in the length of Zr–O bonds, which may result in the continuous decrease in wavenumber for the band P9 on each side of the stoichiometric composition.

On the other hand, as seen in Fig. 5, the intensities of various bands also show some interesting trends of variation with composition. Generally, with increasing $SmO_{1.5}$, the intensities of the bands with low wavenumbers increase, whereas the intensities of those with high wavenumbers decrease, which is attributed to the correlation between the Raman shift and various chemical bonds, as discussed above. Among them, the intensity of the band P4 varies little with composition. This band with an intermediate wavenumber may be a combination of the vibrations of Zr–O and Sm–O bonds. To eliminate the effect of measurement conditions, the relative intensities of various bands compared with the band P4 are summarized in Fig. 8.

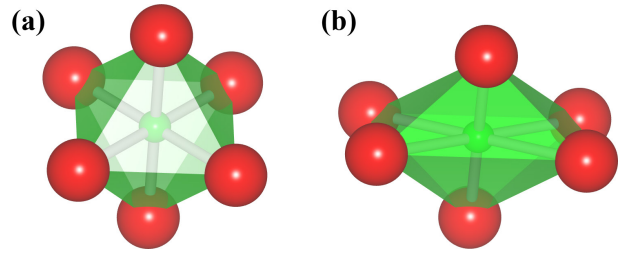

Fig. 7 Distortion of BO_6 octahedra in $A_2B_2O_7$ pyrochlore with increase of the positional parameter *x*, which varies from (a) a regular BO_6 octahedron for ideal pyrochlore with $x = 0.3125$ to (b) a much more distorted BO_6 octahedron for fluorite with $x = 0.375$. Red spheres represent oxygen anions, green spheres represent B cations, such as, Zr ions, and green translucent octahedra stand for BO_6 octahedra.

As shown in Fig. 8(a), the relative intensities of the bands P2 and P3 exhibit opposite variation tendencies in the pyrochlore phase field and phase transition regions. The former shows a significant increase in the intensity within the pyrochlore phase field, approaching a maximum around the stoichiometric composition, whereas the latter exhibits a significant decrease in the intensity within this field, with a minimum around the stoichiometric composition. On the other hand, it can be seen from Fig. 8(b) that the relative intensities of the bands P6 and P7 show a similar decreasing trend with increasing $SmO_{1.5}$ content, except for a local increase in the band P6 observed around the stoichiometric composition. Moreover, the band P5 also decreases in intensity with increasing $SmO_{1.5}$ until it disappears at the stoichiometric composition, whereas the band P8 appears and increases with increasing $SmO_{1.5}$ excess. The band P9, which is not shown here, has a very low intensity and seems to decrease slightly in the pyrochlore phase field, achieving a minimum around the stoichiometric composition.

Besides the influence of measurement parameters and the surface enhancement of Raman scattering, the intensity of Raman bands is mainly determined by the number and polarizability of the corresponding vibrational bonds. The opposite variation tendencies of the intensities of the bands P2 and P3 can be attributed to the difference in the vibrations related to two different O ions at the 48*f* site and 8*b* site in the pyrochlore. Since both the excess Sm^{3+} ions and the excess Zr^{4+} ions alter the surrounding chemical environment of 48*f* O ions within Sm_2Zr_2 tetrahedra, the number of O ions at this site should reach a maximum at the stoichiometric composition. Moreover, the minimum position parameter *x* at the stoichiometric composition leads to more distortion of SmO_8 cube and thus increases the polarizability of the bonds. Therefore, the band P2 can be identified to involve the vibrations of the bonds between Sm ions and 48*f* O ions. Accordingly, the band P3 could be considered to involve the vibrations of the bonds between Sm ions and 8*b* O ions. The excess Sm^{3+} ions may increase the number of 8*b* O ions surrounded by four Sm^{3+} ions and could be chiefly responsible for

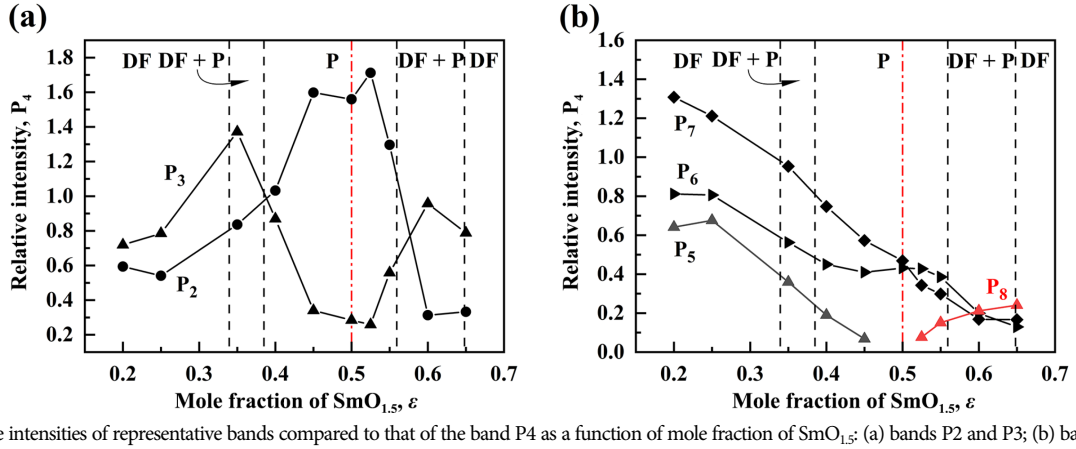

Fig. 8 Relative intensities of representative bands compared to that of the band P4 as a function of mole fraction of $SmO_{1.5}$: (a) bands P2 and P3; (b) bands P5, P6, P7, and P8. The phase boundaries verified by XRD are indicated in the figures to confirm the variation due to the phase transition. The connecting line is a guide to the eye.

the increase in the intensity of the band P3 on the right side of the stoichiometric composition. The excess Zr^{4+} ions may also change the next nearest neighbor of 8*b* O ions and increase the polarizability of the bonds between Sm ions and 8*b* O ions, which would result in an increase in intensity on the left side of the stoichiometric composition.

The decrease in the relative intensities of the bands with high wavenumbers, such as bands P6 and P7, can be easily attributed to the decrease in the number of Zr–O bonds due to the decrease in the number of Zr ions with increasing $SmO_{1.5}$. The similar decrease in the intensity of the band P5, as well as its subsequent disappearance, is considered to be a result of the decrease in the number of Zr ions and particularly the gradual disappearance of 8*a* O interstitials. In addition, the local increase at approximately $\varepsilon = 0.500$ in the case of the band P6 may be attributed to the increase in the number of 48*f* O ions or in the polarizability of Zr–O bonds due to the varying distortion of ZrO_6 octahedra. Conversely, the slight decrease in the intensity of the band P9 around the stoichiometric composition may also be attributed to the distortion of ZrO_6 octahedra. As shown in Fig. 7, the variation in the distortion of the octahedron increases the angles of some O-Zr-O bonds but simultaneously decreases those of others, which may induce different variations in the polarizability. On the other hand, the anomalous increase in the intensity of the band P8 with increasing $SmO_{1.5}$ is believed to be a result of the generation of a new point defect and its continuous increase in number.

Generally, Raman line broadening can indicate the degree of structural disorder or lattice strain [37,48]. As shown in Fig. 9, full widths at half maximum (FWMHs) of all the representative bands, except the band P9, reach their minimum around the stoichiometric composition, which implies that the nonstoichiometry remarkably increases the structural disorder in the pyrochlore phase field. The abnormal variation in the only band P9 may be attributed to the different impacts of the distortion of ZrO_6 octahedron, as discussed above, or just to the fitting error due to the extremely low intensity. Furthermore, comparing the variations in all the bands in detail, we can see that the FWMHs of the bands with relatively low wavenumbers, such as the bands P2 and P3, show more pronounced V-shaped variations in the pyrochlore phase field, whereas the FWMHs of those with high wavenumbers, such as the bands P6 and P7, vary asymmetrically on each side of the stoichiometric composition, which suggests that the different responses of Sm–O and Zr–O bonds to nonstoichiometry. Interestingly, when the composition transforms from a defective fluorite structure to a pyrochlore structure on both sides, the bands P2 and P3 distinctly broaden, whereas the bands P6 and P7 narrow accordingly. This can be interpreted that SmO_8 cube in fluorite is badly distorted during the transition, whereas ZrO_6 polyhedron tends to be a more regular octahedron at the same time. Moreover, the band P4 shows a combined behavior that is similar to those of the bands P2 and P3 on the left side of the stoichiometric composition but is similar to those of the bands P6 and P7 on the other side, which further demonstrates that this band involves the vibrations of both Zr–O and Sm–O bonds.

3.3 Defect chemistry and solution mechanism

As mentioned above, nonstoichiometry introduces various point defects that can significantly reduce thermal conductivity. However, identifying the exact types of point defects is difficult. The theoretical simulation, which is based on energy minimization and valence balance, can predict the possible solution mechanisms, but the variety of the defect reactions and the calculation errors originating from the modeling problems and approximation reduce the reliability of the simulations. It is essential to verify the possible solution mechanisms with experimental results.

In our previous work [43], an experimental method was proposed to confirm the solution mechanism by comparing the variation trends of the experimental densities and the theoretical densities calculated on the basis of various defect reaction models. In this work, this method was used to verify several possible solution mechanisms that were proposed in light of Ref. [29] and the above analysis of Raman spectra. Owing to the difficulty of sintering, especially for the compositions with excess $SmO_{1.5}$, it is difficult to obtain fully dense samples. Several attempts have been made, and more than four series of samples have been prepared using different pressing and sintering processes. Their densities were measured and summarized, as shown in Fig. 10.

The defect reaction models proposed by Stanek *et al.* [29] were first considered. In the case of BO_2 excess, their calculation results implied that pyrochlores prefer to take the A cation vacancies as compensating defects, whereas there is another competing defect mechanism in defective fluorites involving oxygen interstitials in addition to the one with the A cation vacancies, both reactions of which have similar energies. These two competing defect mechanisms can be represented in Kröger–Vink notation as Eqs. (6) and (7) [29]:

$$7BO_2 \xrightarrow{2A_2B_2O_7} 3B_A^{\cdot} + V_A^{'''} + 4B_B + 14O_O \quad (6)$$

$$4BO_2 \xrightarrow{A_2B_2O_7} 2B_A^{\cdot} + 2B_B + 7O_O + O_i^{''} \quad (7)$$

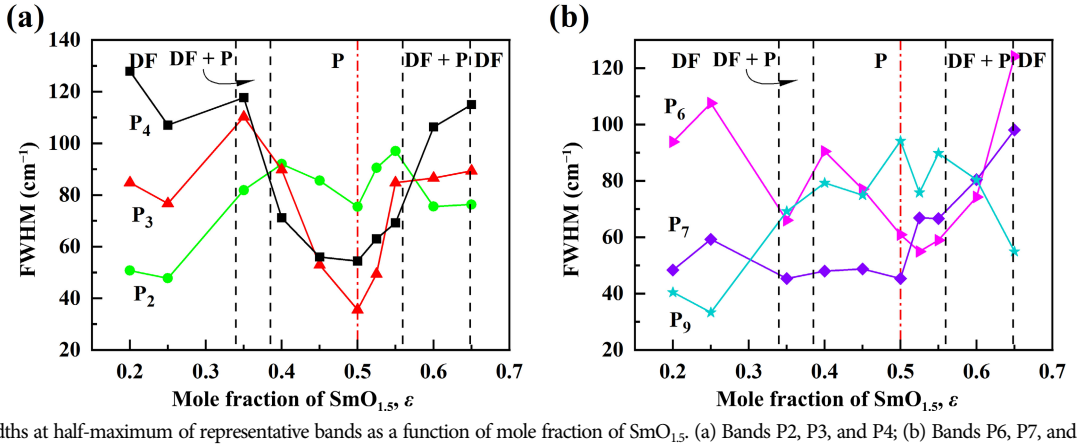

Fig. 9 Full widths at half-maximum of representative bands as a function of mole fraction of $SmO_{1.5}$. (a) Bands P2, P3, and P4; (b) Bands P6, P7, and P9. The phase boundaries verified by XRD are indicated in the figures to confirm the variation due to the phase transition. The connecting line is a guide to the eye.

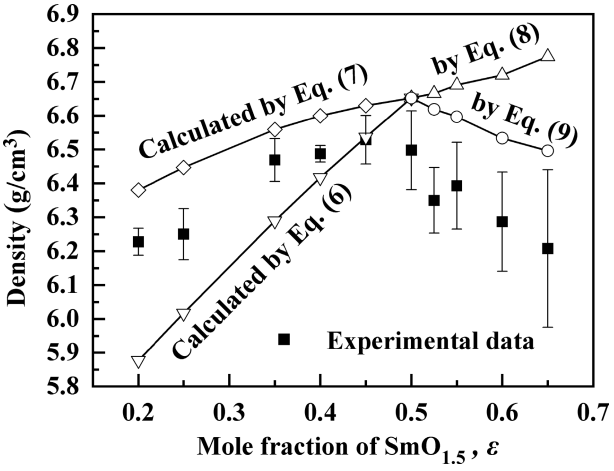

Fig. 10 Comparison of experimental densities of samples with possible theoretical densities. Theoretical densities were calculated based on various defect reaction models Eqs. (6)–(9), as well as lattice parameters obtained in this work. The connecting line is a guide to the eye.

Stanek *et al.* [29] deduced that the counterintuitive defect mechanism (Eq. (6)) in pyrochlores with BO_2 excess may be attributed to the distinct structure of the pyrochlore from that of the defective fluorite. However, our experimental data do not support this deduction or their calculation results. First, the nearly linear variation in the lattice parameters and the continuous variation in the Raman spectra across the phase transition regions suggest that there is only a slight distinction between the pyrochlore and defective fluorite structures. In contrast, the complete difference in the Raman spectra between the defective fluorites and the ideal fluorite indicates that the so-called defective fluorite structure is more than a fluorite but closer to a pyrochlore structure, which is actually more appropriately defined as a disordered pyrochlore. Second, the appearance of the band P5 in the Raman spectra is believed to demonstrate the existence of interstitial oxygen occupying the 8*a* sites, as indicated in Eq. (7). Third, as shown in Fig. 10, the model corresponding to Eq. (6) significantly underestimates the theoretical densities, which are even lower than the experimental data when $\varepsilon < 0.500$. In contrast, the theoretical densities calculated via Eq. (7) show a similar variation trend as the experimental data. Moreover, there is no distinguishing turning point within the phase transition regions. This demonstrates that the nonstoichiometry associated with excess ZrO_2 in $SmO_{1.5}$–ZrO_2 system follows the defect mechanism involving interstitial oxygen, whether in pyrochlores or defective fluorites, which is not consistent with the calculation results of Stanek *et al.* [29].

In the case of $AO_{1.5}$ excess, Stanek *et al.* [29] predicted an explicit defect mechanism involving oxygen vacancies over the entire compositional range, which can be represented as Eq. (8):

$$4AO_{1.5} \xrightarrow{A_2B_2O_7} 2A_A + 2A_B^{'} + V_O^{\cdot\cdot} + 6O_O \quad (8)$$

However, it can be seen from Fig. 10 that this model seems to overestimate the theoretical densities compared with the experimental data. The experimental data show a significant decrease with increasing $SmO_{1.5}$, but the theoretical densities calculated via Eq. (8) increase instead. It appears that introducing only oxygen vacancies is not sufficient to reduce the theoretical density because the atomic weight of Sm ions is much greater than that of Zr ions. To determine the most likely solution mechanism, several defect models have been proposed and verified by comparing the corresponding theoretical densities with the experimental densities. The model in the best agreement can be represented as Eq. (9):

$$7AO_{1.5} \xrightarrow{2A_2B_2O_7} 4A_A + 3A_B^{'} + V_B^{''''} + 3.5\,V_O^{\cdot\cdot} + 10.5O_O \quad (9)$$

In this model, the B cation vacancies are introduced to accommodate the excess $AO_{1.5}$ in addition to the oxygen vacancies. Alternatively, the A cation vacancies could also be the possible compensating defects to satisfy the variation in density, but some evidence suggests that the B cation vacancies are more appropriate. First, it seems fairly natural for the A cations to preferentially take their original crystallographic site when they are in excess, which is favorable for maintaining the valence balance. Second, the appearance of the band P8 in the Raman spectra may be evidence of the existence of Zr ion vacancies. As shown in Fig. 6, the band P8 appears only on the right side of the stoichiometric composition with high wavenumbers. Similar to the other special band P5, the appearance on only one side implies the existence of a distinctive point defect due to the corresponding nonstoichiometry, whereas the relatively high wavenumber indicates that it may also involve Zr–O bonds. Moreover, the band P8 appears to split from the band P7, which provides further evidence for its association with Zr–O bond. The absence of Zr ion in Sm_2Zr_2 tetrahedron, i.e., Zr ion vacancy, may lead to the strengthening of other Zr–O bonds, which results in the appearance of the band P8 and its unusual increase in intensity with increasing $SmO_{1.5}$.

Hence, the solution mechanism for the nonstoichiometric nature of $SmO_{1.5}$–ZrO_2 system involves oxygen interstitials at 8*a* site for excess ZrO_2 (Eq. (7)) and involves Zr ion vacancies and oxygen vacancies for excess $SmO_{1.5}$ (Eq. (9)), in addition to cation antisites for both cases. The calculated theoretical densities in terms of this mechanism are in good agreement with the experimental data and can be used to calculate the relative densities and porosities for thermal conductivity measurements.

3.4 Thermal conductivity and phonon mean free path

The thermal conductivities of all the investigated samples in $SmO_{1.5}$–ZrO_2 system, which was calculated from the measured thermal diffusivities and densities via Eq. (1) and corrected via Eq. (2), are plotted in Fig. 11 as a function of mole fraction of

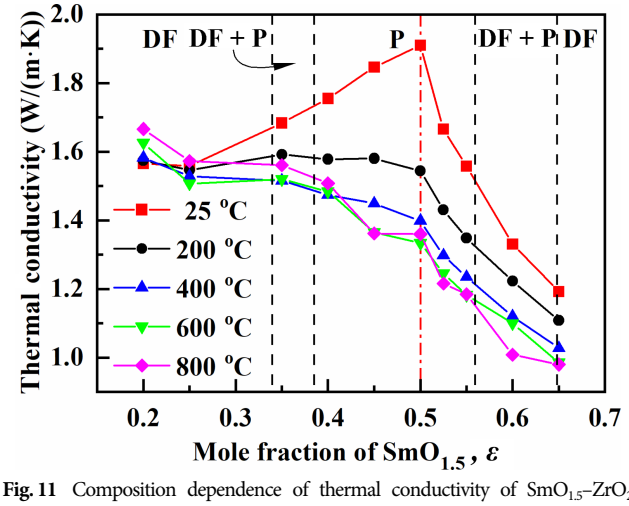

Fig. 11 Composition dependence of thermal conductivity of $SmO_{1.5}$–ZrO_2 system at various temperatures. The overall uncertainty of thermal conductivity is estimated to be less than ±5% at each of the temperatures, and error bars are not shown here for clarity. The phase boundaries verified by XRD are indicated in the figure to confirm the variation due to the phase transition. The connecting line is a guide to the eye.

$SmO_{1.5}$. The most remarkable feature of the data is the distinctiveness of the thermal conductivity variation at room temperature compared with the cases at higher temperatures. At room temperature, the thermal conductivity within the pyrochlore phase field and the two-phase regions shows an inverted V-shaped variation with composition, reaching its maximum at the stoichiometric composition. This implies that the nonstoichiometry on both sides dramatically reduces the thermal conductivity at room temperature, although the thermal conductivity on the right side decreases more rapidly than that on the left side. However, with increasing temperature, this trend changes quickly; even at 200 °C, the thermal conductivity slightly increases on the left side, whereas it still decreases on the other side. This change in the trend leads to an intersection of the temperature-dependent curves of the stoichiometric composition and nonstoichiometric compositions on the ZrO_2-rich side, as reported by Liu *et al.* [21,22]. Moreover, there is a local extreme point at the composition with $\varepsilon = 0.250$, which lies near the boundary of the defective fluorite phase field and close to the left two-phase region. At this point, the thermal conductivity is relatively lower than that on both sides, which corresponds to the turning point between the rapidly decreasing curve on the left side and the bulge in the vicinity of the pyrochlore phase field, as reported by Wu *et al.* [19]. Accordingly, it can be inferred that there could also be a local extreme point on the right side, which may be at a composition near $\varepsilon = 0.650$. Unfortunately, we did not investigate the thermal conductivities of the samples within the right defective fluorite phase field. Furthermore, the temperature dependence of the thermal conductivity varies with the composition. For the compositions with a defective fluorite structure, the thermal conductivity of the composition with $\varepsilon = 0.200$ slightly increases with temperature, whereas that of the composition with $\varepsilon = 0.250$ is almost temperature-independent. For the compositions within the pyrochlore phase field and the two-phase regions, the temperature dependence varies from an approximate $1/T$ variation for the stoichiometric composition to a variation that is much less pronounced along with the deviation from stoichiometry.

To understand the interesting variation with composition, the data were further investigated in terms of the phonon-scattering theory. Analogous to the kinetic theory of gases, Debye described the thermal conduction in dielectric solids as the transport of phonons carrying energy, and the thermal conductivity can be represented in another form Eq.(10) [49], which is equivalent to Eq. (1):

$$\kappa' = \frac{1}{3} \cdot c_V \cdot \bar{v} \cdot l \tag{10}$$

where c_V and l represent the heat capacity per unit volume and the phonon mean free path, respectively. The volumetric heat capacity (c_V) slightly decreases with the composition ε and slightly increases with temperature, which contributes little to the variation in the thermal conductivity. The average velocity of phonon ($\bar{v}$) was calculated via Eq. (3) in terms of the longitudinal and transverse acoustic speeds measured via the ultrasonic reflection method, as shown in Fig. 12(a). The average velocity of phonons remains almost constant for the compositions on the left side of the stoichiometric composition but decreases dramatically for the compositions on the right side. As we know, the average acoustic velocity can be estimated from Young's modulus (E) and density (ρ) via Eq. (11) [35]:

$$\bar{v} = C\sqrt{\frac{E}{\rho}} \tag{11}$$

where C is approximated to be 0.87±0.02. Since Young's modulus is closely related to the crystal energy, the steady value of the average acoustic velocity, as well as the increase in density on the ZrO_2-rich side, indicates a slight increase in the crystal energy, which may be attributed to the tighter structure with less disorder and defects when approaching the stoichiometric composition. On the other hand, the dramatic decrease in the average acoustic velocity on the $SmO_{1.5}$-rich side suggests a sharp drop in the crystal energy, which may be the result of the increasing number of oxygen vacancies and Zr ion vacancies due to the excess $SmO_{1.5}$, as indicated in Eq. (9).

The phonon mean free path can be derived by combining Eqs. (1) and (10), as well as the relation $c_p \cdot \rho = c_V$, which can be expressed as Eq. (12):

$$l = 3\lambda / \bar{v} \tag{12}$$

The derived values of the phonon mean free path of all the investigated samples are shown in Fig. 12(b). At room temperature, the phonon mean free path within the pyrochlore phase field and the two-phase regions shows a more symmetrical inverted V-shaped variation with composition than the thermal conductivity does, which indicates that the dramatic decrease in the average acoustic velocity is chiefly responsible for the more rapid decrease in the thermal conductivity on the right side. On the other hand, as the temperature increases, the variation trend of the phonon mean free path also shows a dramatic change, which is similar to the case of the thermal conductivity. The phonon mean free path decreases rapidly to be almost completely independent of the composition above 200 °C, showing a slight and continuous decrease with increasing $SmO_{1.5}$ across the entire composition range. Considering the variation in the average acoustic velocity, it can be inferred that at high temperatures, the slight increase in the thermal conductivity with deviation from the stoichiometry on the left side can be attributed to the slight variation in the phonon mean free path, whereas the dramatic decrease on the right side is primarily the result of the similar variation in the average acoustic velocity. When the temperature exceeds 600 °C, the phonon mean free path appears to be temperature independent in addition to almost completely composition independent and approaches the bond length of Sm–48*f* O (~2.51 Å). This value is close to the theoretical limit value, which indicates that the thermal conductivity has reached its minimum.

Moreover, the remarkable variation in the phonon mean free path at room temperature, as well as the dramatic change in the variation trend at higher temperatures, can be attributed to the contributions of various phonon scattering processes. The phonon mean free path in dielectric solids is chiefly determined by three scattering processes: the intrinsic Umklapp process, defect scattering, and boundary scattering. It can be represented by Eq. (13):

$$\frac{1}{l} = \frac{1}{l_i} + \frac{1}{l_p} + \frac{1}{l_b} \tag{13}$$

where l_i, l_p, and l_b represent the phonon mean free paths corresponding to the Umklapp scattering, the defect scattering, and the boundary scattering, respectively. Since the grain sizes of all the samples in this work are several orders of magnitude larger than the phonon mean free path, the contribution of the

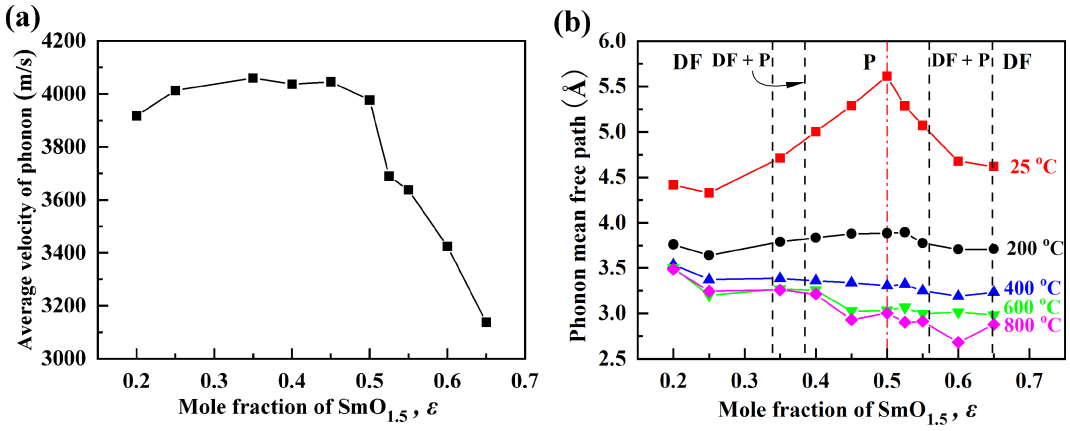

Fig. 12 (a) Average velocity and (b) mean free path of phonon of all the investigated samples. The phase boundaries verified by XRD are indicated in the figure (b) to confirm the variation due to the phase transition. The connecting line is a guide to the eye.

boundary scattering can be ignored. On the other hand, the phonon mean free paths corresponding to the Umklapp scattering and defect scattering can be expressed as Eqs. (14) and (15) [19,44]:

$$l_i = \frac{\mu\Omega v_t \omega_D}{2\gamma^2 k_B N^{1/3}} \cdot \omega^{-2} T^{-1} \tag{14}$$

$$l_p = \frac{4\pi v_t^4}{\Omega\Gamma} \cdot \omega^{-4} \tag{15}$$

where μ, Ω, ω_D, γ, k_B, N, Γ, ω, and T represent the shear modulus, the average atomic volume, the Debye frequency, the Grüneisen anharmonicity parameter, the Boltzmann constant, the number of atoms per molecule, the imperfection scattering parameter representing the strength of point defect phonon scattering, the frequency of phonons, and the absolute temperature, respectively. It can be easily observed that the phonon mean free path corresponding to the Umklapp scattering varies in inverse proportion to the absolute temperature, whereas that due to the defect scattering is independent of temperature at moderately high temperatures, generally above half of the Debye temperature [50]. As a result, the contribution of the defect scattering is expected to weaken significantly with increasing temperature. Thus, the nearly composition independence at high temperatures may be attributed to the Umklapp scattering, whereas the significant reduction in the phonon mean free path with nonstoichiometry at room temperature may be primarily determined by the defect scattering.

Furthermore, the relative effectiveness of various defects on phonon scattering is somewhat surprising. Particularly for the case of excess ZrO_2, as discussed above, the introduced oxygen interstitials with nonstoichiometry occupy the 8*a* vacancy site that is usually regarded as a strong scattering center of phonons. This means that the concentration of the so-called intrinsic "oxygen vacancies" at 8*a* sites is significantly reduced, and the scattering of phonons is expected to weaken, which would lead to an increase in the phonon mean free path as well as the thermal conductivity. However, this is not the case in our results. The significant reduction in the phonon mean free path and the thermal conductivity further demonstrates the conclusion in our previous work [44] that the so-called "oxygen vacancies" at 8*a* sites, which satisfy the periodicity of the crystal, are not effective scattering centers for phonons. In other words, the ordered unoccupied 8*a* sites in pyrochlore are not point defects at all. Instead, the interstitial oxygen ions occupying 8*a* sites are actually the defects that scatter the phonons and decreases the thermal conductivity at room temperature. Notably, the relative effectiveness of the 8*a* oxygen interstitials on phonon scattering appears to be very close to that of the Zr ion vacancies and oxygen vacancies for the case of $SmO_{1.5}$ excess.

4 Conclusions

In this work, a series of solid solutions of $\varepsilon SmO_{1.5}$·$(1-\varepsilon)ZrO_2$ (ε = 0.200, 0.250, 0.350, 0.400, 0.450, 0.500, 0.525, 0.550, 0.600, and 0.650) were designed and synthesized to investigate the effects of nonstoichiometry on the structural evolution, defect chemistry, and thermal conductivity of $SmO_{1.5}$–ZrO_2 system across the entire pyrochlore phase field and phase transition regions. As evidenced by XRD and Raman spectra, the phase transition from pyrochlore to defective fluorite does not lead to a dramatic structural change. The resolved Raman spectra, in terms of their similarity to each other, further demonstrate the distinct structural evolution on each side of the stoichiometric composition as well as the emergence of the expected point defects. A new solution mechanism was then proposed and confirmed by analyzing the variation in the experimental density and Raman spectra. This mechanism involves interstitial oxygen at the 8*a* site for excess ZrO_2 and involves Zr ion vacancies and oxygen vacancies for excess $SmO_{1.5}$, in addition to cation antisites.

The thermal conductivities of all the compositions were measured and investigated in terms of the phonon-scattering theory. The results show that the nonstoichiometry with $SmO_{1.5}$ excess is more effective in reducing the thermal conductivity, which can be attributed to the dramatic decrease in the average acoustic velocity in addition to the strong phonon scattering of the Zr ion vacancies and oxygen vacancies, as indicated by the above solution mechanism. On the other hand, the nonstoichiometry with ZrO_2 excess significantly reduces the thermal conductivity at room temperature but leads to a slight increase above 200 °C. The former variation can be attributed to the phonon scattering of the 8*a* oxygen interstitials, which are actually the defects scattering the phonons and decreasing the thermal conductivity, rather than so-called intrinsic "oxygen vacancies". The relative effectiveness of the 8*a* oxygen interstitials on phonon scattering appears to be very close to that of the Zr ion vacancies and oxygen vacancies in the case of $SmO_{1.5}$ excess. Moreover, the latter variation may be attributed to the Umklapp scattering.

Acknowledgements

This work was supported by the National Natural Science Foundation of China (No. 52172062) and the YEQISUN Joint Funds of the National Natural Science Foundation of China (No. U2241279).

Declaration of competing interest

The authors have no competing interests to declare that are relevant to the content of this article. The author Wei Pan is the Associate Editor of this journal. The author Zhixue Qu is the Editorial Committee member of this journal.

References

[1] Vassen R, Cao XQ, Tietz F, *et al.* Zirconates as new materials for thermal barrier coatings. *J Am Ceram Soc* 2000, **83**: 2023–2028.

[2] Padture NP, Gell M, Jordan EH. Thermal barrier coatings for gas-turbine engine applications. *Science* 2002, **296**: 280–284.

[3] Cao XQ, Vassen R, Stoever D. Ceramic materials for thermal barrier coatings. *J Eur Ceram Soc* 2004, **24**: 1–10.

[4] Pan W, Phillpot SR, Wan CL, *et al.* Low thermal conductivity oxides. *MRS Bull* 2012, **37**: 917–922.

[5] Wei ZY, Meng GH, Chen L, *et al.* Progress in ceramic materials and structure design toward advanced thermal barrier coatings. *J Adv Ceram* 2022, **11**: 985–1068.

[6] Wan CL, Pan W, Xu Q, *et al.* Effect of point defects on the thermal transport properties of $(La_xGd_{1-x})_2Zr_2O_7$: Experiment and theoretical model. *Phys Rev B* 2006, **74**: 144109.

[7] Liu ZG, Ouyang JH, Zhou Y. Preparation and thermophysical properties of $(Nd_xGd_{1-x})_2Zr_2O_7$ ceramics. *J Mater Sci* 2008, **43**: 3596–3603.

[8] Wan CL, Zhang W, Wang YF, *et al.* Glass-like thermal conductivity in ytterbium-doped lanthanum zirconate pyrochlore. *Acta Mater* 2010, **58**: 6166–6172.

[9] Wan CL, Qu ZX, Du AB, *et al.* Order–disorder transition and unconventional thermal conductivities of the $(Sm_{1-x}Yb_x)_2Zr_2O_7$ series. *J Am Ceram Soc* 2011, **94**: 592–596.

[10] Wang YF, Yang F, Xiao P. Glass-like thermal conductivities in $(La_{1-x1}Y_{x1})_2(Zr_{1-x2}Y_{x2})_2O_{7-x/2}$ ($x = x1 + x2$, $0 \le x \le 1.0$) solid solutions. *Acta Mater* 2012, **60**: 7024–7033.

[11] Guo L, Li BW, Cheng YX, *et al.* Composition optimization, high-temperature stability, and thermal cycling performance of Sc-doped $Gd_2Zr_2O_7$ thermal barrier coatings: Theoretical and experimental studies. *J Adv Ceram* 2022, **11**: 454–469.

[12] Li F, Zhou L, Liu JX, *et al.* High-entropy pyrochlores with low thermal conductivity for thermal barrier coating materials. *J Adv Ceram* 2019, **8**: 576–582.

[13] Pitike KC, Macias A, Eisenbach M, *et al.* Computationally accelerated discovery of high entropy pyrochlore oxides. *Chem Mater* 2022, **34**: 1459–1472.

[14] Wright AJ, Luo J. A step forward from high-entropy ceramics to compositionally complex ceramics: A new perspective. *J Mater Sci* 2020, **55**: 9812–9827.

[15] Xiang HM, Xing Y, Dai FZ, *et al.* High-entropy ceramics: Present status, challenges, and a look forward. *J Adv Ceram* 2021, **10**: 385–441.

[16] Liu DB, Shi BL, Geng LY, *et al.* High-entropy rare-earth zirconate ceramics with low thermal conductivity for advanced thermal-barrier coatings. *J Adv Ceram* 2022, **11**: 961–973.

[17] Luo XW, Huang RQ, Xu CH, *et al.* Designing high-entropy rare-earth zirconates with tunable thermophysical properties for thermal barrier coatings. *J Alloys Compd* 2022, **926**: 166714.

[18] Zhao M, Pan W, Wan CL, *et al.* Defect engineering in development of low thermal conductivity materials: A review. *J Eur Ceram Soc* 2017, **37**: 1–13.

[19] Wu J, Padture NP, Klemens PG, *et al.* Thermal conductivity of ceramics in the ZrO_2–$GdO_{1.5}$ system. *J Mater Res* 2002, **17**: 3193–3200.

[20] Chen Q, Xie Y, Yan ZX, *et al.* Impact of nonstoichiometry on the mechanical properties and thermal conductivity of gadolinium zirconate ceramics. *Ceram Int* 2023, **49**: 33972–33980.

[21] Liu ZG, Ouyang JH, Wang BH, *et al.* Preparation and thermophysical properties of $Nd_xZr_{1-x}O_{2-x/2}$ ($x = 0.1, 0.2, 0.3, 0.4, 0.5$) ceramics. *J Alloys Compd* 2008, **466**: 39–44.

[22] Liu ZG, Ouyang JH, Wang BH, *et al.* Thermal expansion and thermal conductivity of $Sm_xZr_{1-x}O_{2-x/2}$ ($0.1 \le x \le 0.5$) ceramics. *Ceram Int* 2009, **35**: 791–796.

[23] Guo L, Zhang Y, Ye FX. Phase structure evolution and thermo–physical properties of nonstoichiometry $Nd_{2-x}Zr_{2+x}O_{7+x/2}$ pyrochlore ceramics. *J Am Ceram Soc* 2015, **98**: 1013–1018.

[24] Wang C, Zinkevich M, Aldinger F. Experimental investigation and thermodynamic modeling of the ZrO_2–$SmO_{1.5}$ system. *J Am Ceram Soc* 2007, **90**: 2210–2219.

[25] Wang C, Zinkevich M, Aldinger F. Phase diagrams and thermodynamics of rare-earth-doped zirconia ceramics. *Pure Appl Chem* 2007, **79**: 1731–1753.

[26] Jorba MPy. Contribution to the research of rare earth-zirconia system. *Ann Chim* 1962, **7**: 479–511. (in French)

[27] Lakiza S, Fabrichnaya O, Wang C, *et al.* Phase diagram of the ZrO_2–Gd_2O_3–Al_2O_3 system. *J Eur Ceram Soc* 2006, **26**: 233–246.

[28] Tabira Y, Withers RL. Structure and crystal chemistry as a function of composition across the wide range nonstoichiometric $(1-\varepsilon)$ $ZrO_2{\cdot}\varepsilon SmO_{1.5}$, $0.38 < \varepsilon < 0.55$, oxide pyrochlore system. *J Solid State Chem* 1999, **148**: 205–214.

[29] Stanek CR, Minervini L, Grimes RW. Nonstoichiometry in $A_2B_2O_7$ pyrochlores. *J Am Ceram Soc* 2002, **85**: 2792–2798.

[30] Lakiza S, Lopato L. Phase diagram of the alumina–zirconia–samaria system. *J Am Ceram Soc* 2006, **89**: 3516–3521.

[31] Mehling H, Hautzinger G, Nilsson O, *et al.* Thermal diffusivity of semitransparent materials determined by the laser-flash method applying a new analytical model. *Int J Thermophys* 1998, **19**: 941–949.

[32] Barin I. *Thermochemical Data of Pure Substances*. Weinheim (Federal Republic of Germany): Wiley, 1995.

[33] Wu J, Wei XZ, Padture NP, *et al.* Low-thermal-conductivity rare-earth zirconates for potential thermal-barrier-coating applications. *J Am Ceram Soc* 2002, **85**: 3031–3035.

[34] Schlichting KW, Padture NP, Klemens PG. Thermal conductivity of dense and porous yttria-stabilized zirconia. *J Mater Sci* 2001, **36**: 3003–3010.

[35] Clarke DR. Materials selection guidelines for low thermal conductivity thermal barrier coatings. *Surf Coat Tech* 2003, **163**: 67–74.

[36] Nandi C, Jain D, Grover V, *et al.* ZrO_2–$NdO_{1.5}$ system: Investigations of phase relation and thermophysical properties. *Mater Design* 2017, **121**: 101–108.

[37] Hess NJ, Begg BD, Conradson SD, *et al.* Spectroscopic investigations of the structural phase transition in $Gd_2(Ti_{1-y}Zr_y)_2O_7$ pyrochlores. *J Phys Chem B* 2002, **106**: 4663–4677.

[38] Shimamura K, Arima T, Idemitsu K, *et al.* Thermophysical properties of rare-earth-stabilized zirconia and zirconate pyrochlores as surrogates for actinide-doped zirconia. *Int J Thermophys* 2007, **28**: 1074–1084.

[39] Shamblin J, Feygenson M, Neuefeind J, *et al.* Probing disorder in isometric pyrochlore and related complex oxides. *Nat Mater* 2016, **15**: 507–511.

[40] Shamblin J, Tracy CL, Palomares RI, *et al.* Similar local order in disordered fluorite and aperiodic pyrochlore structures. *Acta Mater* 2018, **144**: 60–67.

[41] Drey D, O'Quinn E, Finkeldei S, *et al.* Local ordering in disordered $Nd_xZr_{1-x}O_{2-0.5x}$ pyrochlore as observed using neutron total scattering. *Acta Mater* 2022, **225**: 117590.

[42] Vandenborre MT, Husson E, Chatry JP, *et al.* Rare-earth titanates and stannates of pyrochlore structure; vibrational spectra and force fields. *J Raman Spectrosc* 1983, **14**: 63–71.

[43] Qu ZX, Wan CL, Pan W. Thermal expansion and defect chemistry of MgO-doped $Sm_2Zr_2O_7$. *Chem Mater* 2007, **19**: 4913–4918.

[44] Qu ZX, Wan CL, Pan W. Thermophysical properties of rare-earth stannates: Effect of pyrochlore structure. *Acta Mater* 2012, **60**: 2939–2949.

[45] Sanjuán ML. Raman spectroscopy study of disorder phenomena and size effects in pyrochlores. In: *Pyrochlore Ceramics*. Chowdhury A, Eds. Elsevier, 2022: 95–159.

[46] Turner KM, Tracy CL, Mao WL, *et al.* Lanthanide stannate pyrochlores ($Ln_2Sn_2O_7$; Ln = Nd, Gd, Er) at high pressure. *J Phys-Condens Mat* 2017, **29**: 504005.

[47] Kumar S, Gupta HC. First principles study of zone centre phonons in rare-earth pyrochlore titanates, $RE_2Ti_2O_7$ (RE = Gd, Dy, Ho, Er, Lu; Y). *Vib Spectrosc* 2012, **62**: 180–187.

[48] Scheetz BE, White WB. Characterization of anion disorder in zirconate $A_2B_2O_7$ compounds by Raman spectroscopy. *J Am Ceram Soc* 1979, **62**: 468–470.

[49] Debye P. *Vorträge über die kinetische Theorie der Materie und der Elektrizität*. Leipzig and Berlin: BG Teubner, 1914. (in German)

[50] Klemens PG. Thermal resistance due to point defects at high temperatures. *Phys Rev* 1960, **119**: 507–509.